ADVANCED MATERIALS INTERFACES
www.advmatinterfaces.de

Encapsulating Semiconductor Quantum Dots in Supramolecular Metal-Organic Frameworks for Superior Photocatalytic Hydrogen Evolution

Chen Pan, Jinyu Chao, Fushuang Niu, Songhai Xie, Haoyang Gu, Tianhui Su, Ke Hu, Dan-Wei Zhang, Ke Liu, Guangfeng Liu, Tengfeng Xie, Zhan-Ting Li,* and Liming Zhang**

Solar-to-hydrogen conversion is a sustainable way of producing renewable fuels, yet the efficiency is limited by the poor photo-induced charge-carrier separation on electrode surface. Developing active and stable hydrogen evolution photocatalysts is challenging and entails intelligent material structure design and tailoring. Here, a novel water dispersible supramolecular metal organic framework (SMOF) is employed as a general and high-performance platform to encapsulate CdS quantum dots (QDs) for achieving highly improved solar-induced H_2-production activity. Particularly, the CdS QDs@SMOF heterostructure exhibits an excellent H_2 generation activity of 49.4 μmol h^{-1} (TOF = 47.0/h), exceeding those of most reported heterogeneous metal organic frameworks-based photocatalytic systems. Advanced characterizations disclose that the strong electrostatic interaction and light-induced charge transfer between SMOF and CdS QDs, combined with the high surface area, water dispersible nature, and abundant reactive centers synergistically contribute to this distinguished photocatalytic performance. The work not only demonstrates the water dispersible SMOF can serve as a versatile and effective platform supporting semiconductor to boost the photocatalytic H_2-production performance without co-catalysts, but also paves avenues to the design and synthesis of SMOF-based heterostructures for general catalysis applications.

1. Introduction

The construction of effective catalytic systems to pursue clean and sustainable energy is a top priority given the increasing global energy demands and the growing environmental crisis.[1] Specifically, photocatalytic water splitting using sunlight and semiconductors enables the production of renewable hydrogen gas to supply energy and feedstock for down-stream products, such as hydrocarbons and alcohols.[2–4] However, some critical issues need to be solved to ultimately realize the practical application of such environmentally benign technology.[5] In view of the solar energy utilization, desirable materials as photocatalysts need not only to harvest a broad range of solar spectrum but also to afford an effective photo-induced charge-carrier separation to obtain a highly efficient solar-to-hydrogen (STH) conversion.[6,7] To improve the charge carrier separation, a promising strategy is to develop hierarchical semiconductor composites that ensure the opposite migration of holes and electrons by valence-band and conduction-band offsets.[8,9]

Metal organic frameworks (MOFs), as crystalline and porous materials assembled with metal ions through periodical coordination bonds, have been employed in various areas such as gas storage and separation, catalysis, sensing, drug delivery, and biomedical imaging.[10] Very recently, MOFs-based hybrids were studied as a new class of photoactive materials for solar-induced hydrogen evolution because of their long-range structures, out-standing surface areas, and tunable bandgaps.[11] Despite of the excellent chemical stability and broad spectrum of light absorption from those porous and crystalline organic structures, their solid nature, however, imposes huge limitations such that nearly all catalytic studies have to be performed in a heterogeneous manner.[12] Also, the rigid pore aperture of conventional MOFs restricts the efficient hierarchical materials fabrication because of the limitation toward insertion when using MOFs as host materials.[13] Both of the drawbacks limit the effective charge-carrier separation on the junction of MOFs-based hierarchical materials.[14] Until now, the reports on hydrogen production with MOFs is still limited and the hydrogen production rate as high as 3.0–4.0 μmol h^{-1} has been

C. Pan, J. Chao, F. Niu, S. Xie, H. Gu, T. Su, K. Hu, D. Zhang, Z. Li, L. Zhang
Department of Chemistry and Shanghai Key Laboratory of Molecular Catalysis and Innovative Materials
Fudan University
Shanghai 200438, China
E-mail: zhangdw@fudan.edu.cn; ztli@fudan.edu.cn; zhanglm@fudan.edu.cn

K. Liu
Shanghai Synchrotron Radiation Facility
Shanghai Advanced Research Institute
Chinese Academy of Sciences
Shanghai 201210, China

G. Liu
National Center for Protein Science Shanghai
Shanghai Advanced Research Institute
Chinese Academy of Sciences
Shanghai 201210, China

T. Xie
Institute of Physical Chemistry
College of Chemistry
Jilin University
Changchun 130012, P. R. China

The ORCID identification number(s) for the author(s) of this article can be found under https://doi.org/10.1002/admi.202101678.

DOI: 10.1002/admi.202101678

achieved.[12] However, this hydrogen production rate is far from the expected and not as good as traditional semiconductor photocatalysts such as metal oxides and sulfides.[15] One possible main cause that limits the hydrogen evolution rate of MOFs is the strong recombination of photogenerated electron–hole pairs.[16] Instead of the hydrothermal and solvothermal techniques that generally applied to synthesize MOFs, self-assembly has been demonstrated as a mild strategy to obtain new materials that can achieve different functions, which includes gas adsorption, drug delivery, molecular recognition, and so on.[17] Recently, our group has obtained homogeneous supramolecular organic frameworks (SMOFs) in both 2D and 3D spaces in aqueous solution, with the feature of typical MOFs under mild conditions.[18] Taking the advantages of the water-dispersible nature and flexible pore aperture owning to the self-assembly, we envision such SMOF structure is preferable for constructing hierarchical semiconductor composites for highly efficient solar water splitting.[19]

Herein, we rationally designed a binary nanohybrid photocatalyst composed of water-dispersible SMOF and CdS quantum dots (QDs), which were intelligently assembled together through electrostatic interactions, for superior homogeneous photocatalytic hydrogen production in the presence of triethanolamine (TEOA) as a hole quencher. Distinguished from the conventional MOFs having solid pore apertures, the flexible and changeable assembly behavior of SMOF render it a tunable pore size, making the encapsulation of CdS QDs much more efficient. Detailed examination showed that the CdS QDs@SMOF hybrid exhibit an excellent photocatalytic H_2 evolving rate of 49.4 μmol h^{-1} with a TOF of 47.0/h, which is ≈80 and 110-folds higher than those of the parent CdS QDs and SMOF, respectively, and is in the top rank of photocatalysts for H_2 evolution among various MOFs-based photocatalysts.[12] Detailed characterizations were carried out to get clear proofs of the photocatalytic H_2 evolution mechanism, revealing that the great enhancement of photocatalytic performance is due to the strong interfacial interaction between CdS QDs and SMOF and the efficient charge transfer at the interface, which inhibits the recombination of photogenerated charges and thereby improves their photocatalytic performance. Our findings lend credence to the prospect of SMOF contributing to the design of multifunctional hybrid photocatalysts for efficient and sustainable energy conversion.

2. Results and Discussion

2.1. Fabrication of CdS QDs@SMOF Heterostructure via Electrostatic Interaction

The homogeneous water-dispersible SMOF was fabricated via a self-assembly procedure.[19] We have established that cucurbit[8] uril (CB[8]) can remarkably stabilize the homodimerization of the 4-phenylpyridin-1-ium (PhPy) unit through hydrophobically driven encapsulation in water, following which, Ru-based SMOF were prepared. Typically, the SMOF was fabricated from the self-assembly of a hexarmed $[Ru(bpy)_3]^{2+}$-based precursor (denoted as $[Ru(bpybp)_3]^{2+}$) and CB[8]. The $[Ru(bpybp)_3]^{2+}$complex core, the purity of which is confirmed by ^{1}H-NMR spectra (Figure S1, Supporting Information), is soluble and highly stable in aqueous solution, and its rigid octahedral nature facilitates the formation of a 3D cubic periodic framework through 2:1 encapsulation of appended PhPy units by CB[8] (**Scheme 1**, see more details in Experimental Section). The strong positive Zeta-potential in SMOF is resulted from the positive charge on the vertex of the net, $[Ru(bpybp)_3]^{2+}$ (**Figure 1**a). The dynamic light scattering (DLS) experiment performed in deionized water evidenced a D_H value of 340 nm (with $[Ru(bpybp)_3]^{2+}$/CB[8] = 3, and the concentration of $[Ru(bpybp)_3]^{2+}$ = 5 μM), clearly confirmed the successful self-assembly of large supramolecular entities (Figure S2, Supporting Information). We also observed a continuing enlargement of D_H in response to the increase of $[Ru(bpybp)_3]^{2+}$ concentration. At 100 μM, the D_H increased to 420 nm and at even higher concentrations, the complex began to precipitate. As shown in Figure 1b, the periodicity of the 3D SMOF network in aqueous solution is verified by synchrotron-based small-angle X-ray scattering (SAXS), which displays an obvious peak related to the d-space centered at ≈3.0 nm. This value matches well with (100) spacing (2.9 nm) of the 3D network simulated using Materials Studio (Accelrys Materials Studio Release Notes, Release 7.0, Accelrys Software Inc., San Diego, USA) (shown by the black line in Figure 1b), indicative of the successful synthesis of dispersible periodic SMOF in water. The broadness of the peak is likely due to the dynamic nature of the supramolecular framework in solution. In addition, the microcrystals of SMOF were obtained via slowly evaporating the aqueous solution at ambient temperature, as evidenced by the transmission electron microscopy (TEM) image (Figure 1c). The energy dispersive X-ray spectrum (EDX) further confirms the presence and uniform distribution of C, N, Ru, and Cl elements, in agreement with the chemical compositions (Figure 1d). The corresponding weight contents of these elements are listed in Table S1, Supporting Information.

CdS QDs were synthesized following previous procedures with modified conditions (see more details in Experimental Section).[20] The obtained QDs were observed as a spherical nanoparticle with an average size of 3.8 nm and exposed lattice spacing of 0.33 nm, corresponding to the (111) facet of cubic-structured CdS QDs (Figure 1e). The ligand covering CdS QDs fabricated in our study is 3-mecaptopropionic acid (MPA) with a negative charge in basic solution, which can be confirmed by the Zeta-potential measurement under a wide range of pH values (Figure 1a and Figure S3, Supporting Information). The strong negative Zeta-potential can well explain the single-particle dispersion of CdS QDs in aqueous solution.

The Zeta-potentials of CdS QDs, SMOF, and their mixtures suggest a strong charge attraction in between (Figure 1a). As schematically shown in Scheme 1, this strong electrostatic interaction, together with the hydrophobic nature of the out-sphere ligand of CdS QDs, drives the insertion of CdS QDs into the network of SMOF. Interestingly, the synchrotron-based SAXS profile of CdS QDs@SMOF hybrid aqueous solution containing 5 μM CdS QDs and 30 μM $[Ru(bpybp)_3]^{2+}$ ($[Ru(bpybp)_3]^{2+}$ was applied to represent the concentration of SMOF, similarly hereinafter) affords a strong scattering peak at ≈5.9 nm, corresponding to the (100) crystallographic planes simulated using Materials Studio software (Figure 1f). After incorporating CdS QDs, each edge of SMOF unit cell consists of three

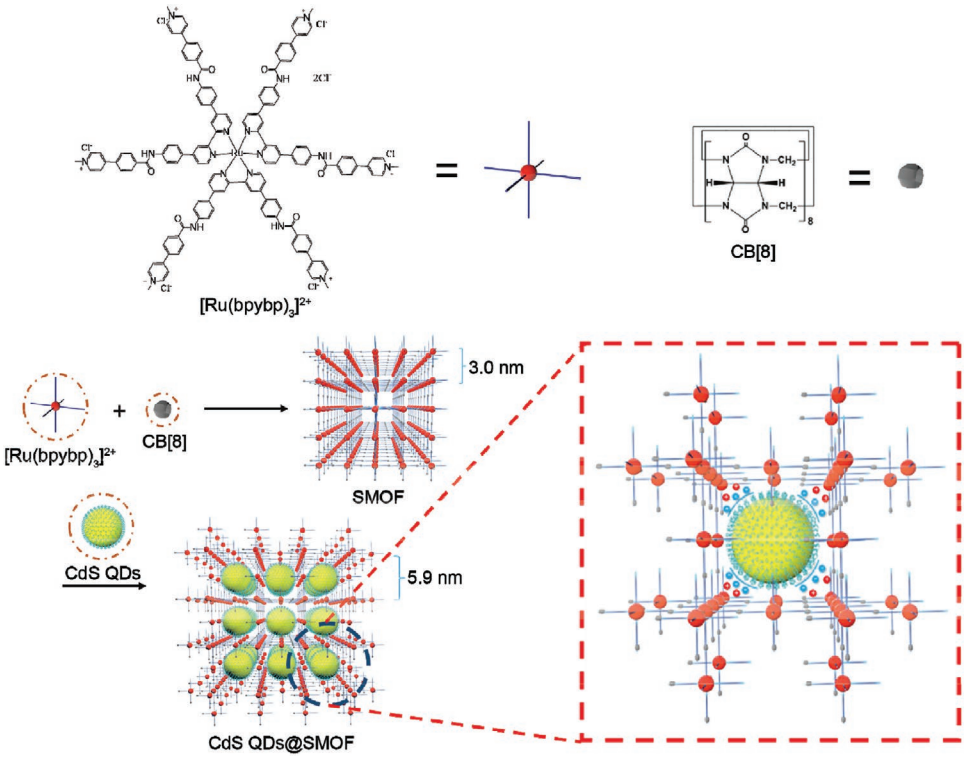

Scheme 1. Schematic illustration of the synthesis of SMOF and CdS QDs@SMOF heterostructure through the self-assembly of a hexarmed $[Ru(bpybp)_3]^{2+}$-based precursor and CB[8] and CdS QDs insertion.

$[Ru(bpybp)_3]^{2+}$ vertexes instead of two in comparison with the as-prepared counterpart, leading to a twofold increase of interplanar spacing of (100) facet (5.9 nm vs 3.0 nm). The pore aperture, defined by the eight CB[8] unit in one self-assembled macrocycle adopting a square-like conformation, was calculated to be ≈4.2 nm. The transformation and rearrangement of SMOF periodicity is probably rationalized by the formation of soft acid ($[Ru(bpybp)_3]^{2+}$)-soft base ($HSCH_2CH_2COO^-$) ion pairs and hard acid (H^+)-hard base (Cl^-) ion pairs. It should be notable that because of the rigid nature of conventional MOFs, insertion of QDs is extremely difficult to achieve if the size distribution of QDs is larger than the pore size of the scaffold.[21] However, the insertion is easily accessible in our system due to the flexible and changeable assembly behavior of SMOF. Accordingly, DLS measurements showed 1.6 times increasing of D_H, from 335 to 505 nm, after the addition of CdS QDs (Figure S4, Supporting Information). It is notable that the dramatic enlargement of D_H at higher concentrations is likely due to the aggregation of SMOF resulted from the weakened charge repulsion after CdS QDs incorporation. Similar with as-prepared SMOF, slow evaporation of the solvent of CdS QDs@SMOF assemblies led to the formation of microcrystals. The SEM and EDX images shown in Figure S5, Supporting Information, clearly evidenced the successful decoration of CdS QDs into SMOF.

2.2. Photocatalytic Hydrogen Generation

Next, CdS QDs@SMOF assemblies were examined for photocatalytic water reduction. In a typical experiment, the CdS QDs@SMOF hybrid was added to a basic aqueous solution (pH 11) containing TEOA as the sacrificial electron donor. TEOA was chosen as an optimized sacrificial agent to capture the photogenerated holes as it demonstrated a dramatically higher H_2 production activity than others, such as lactic acid, methanol, and sulfite (Figure S6, Supporting Information). The reaction mixture was irradiated by a solar simulator source (λ = 350–1100 nm, 100 mW cm^{-2}), and the headspace gas was analyzed on-line by gas chromatography to quantify the amount of H_2 produced. We first investigated the H_2 production efficiency by keeping the concentration of CdS QDs at 5 μM and changing the concentration of $[Ru(bpybp)_3]^{2+}$ from 25 to 125 μM. **Figure 2**a shows optical images of the resultant seven aqueous solution of CdS QDs@SMOF, which display an increasing absorption from blank CdS QDs to blank SMOF. The H_2 evolving rate of a series of hybrid materials exhibit an obvious increase tendency until the mole constitution ratio of CdS QDs: $[Ru(bpybp)_3]^{2+}$ = 1:20. As displayed in Figure 2b, at $[Ru(bpybp)_3]^{2+}$ = 100 μM, the CdS QDs@SMOF hybrid showed a maximum photocatalytic activity of 49.4 μmol h^{-1}, which corresponded to a turnover frequency (TOF) of 47.0/h (based on the mole amounts of CdS QDs and $[Ru(bpybp)_3]^{2+}$), and the apparent quantum yield (AQY) is ≈12% (see more details in Experimental Section). In this case, the level of H_2 production rate is 80 folds higher than that of pure CdS QDs (≈0.61 μmol h^{-1}), and exceeds the parent SMOF (≈0.45 μmol h^{-1}) by almost 110 folds. The performances of both pure CdS and SMOF were limited by their poor charge-separation efficiencies. Further raising $[Ru(bpybp)_3]^{2+}$ concentration arouses a decrease tendency of activity, which may be attributed

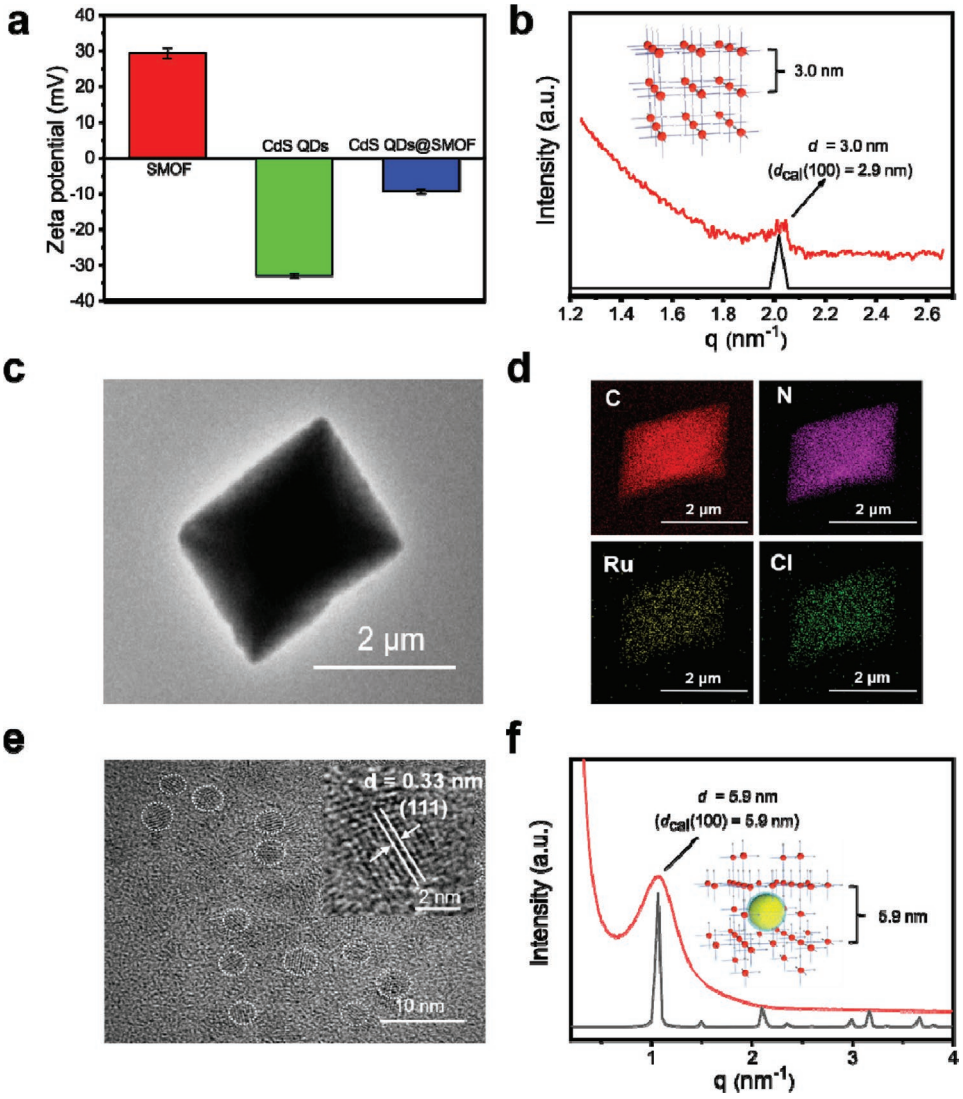

Figure 1. a) Zeta potentials of CdS QDs, SMOF, and CdS QDs@SMOF. b) Solution-phase synchrotron SAXS of SMOF in water (red line) and theory simulation result using Materials Studio 7.0 (black line). Inset shows the schematic illustration of SMOF. c) The TEM and d) EDX elemental mapping [C (red), N (purple), Ru (yellow) and Cl (green)] of a SMOF single particle. e) HRTEM image of CdS QDs, the inset is an enlarged image showing the lattice pattern of CdS QDs, and the interplanar spacing $d = 0.33$ nm is in accordance with the (111) plane of CdS QDs. f) Solution-phase synchrotron SAXS of CdS QDs@SMOF in water (red line) and the theory simulation result using Materials Studio 7.0 (black line). Inset shows the schematic illustration of CdS QDs@SMOF.

to the block of light harvesting to CdS QDs from SMOF. The high H_2 production efficiency of CdS QDs@SMOF hybrid materials could be attributed to their unique encapsulation pattern and homogeneity, which not only allowed for quick diffusion and close contact of water and TEOA molecules, but also facilitated the charge transfer between the excited CdS QDs and $[Ru(bpybp)_3]^{2+}$. The optimum photocatalytic H_2 evolution activity of CdS QDs@SMOF hybrid materials under simulated solar irradiation was studied to evaluate for solar energy conversion, and the STH efficiency was estimated to be ≈1.04 %. In addition, to investigate the influence of electrostatic attraction on activity, we rationally designed the surface ligands of CdS to modify the electrostatic attraction between CdS and SMOF. Surface-ligand-free CdS-BF_4 was synthesized and incorporated with SMOF under an identical condition (see more details in Experimental Section). The hybrid structure CdS-BF_4@SMOF had the similar absorption range, but showed a much poorer activity (6.71 μmol h^{-1}) in relative to CdS-MPA@SMOF (Figure S9, Supporting Information), indicating the great contribution of electrostatic attraction to charge separation.

By keeping CdS QDs: $[Ru(bpybp)_3]^{2+}$ = 1:20, the hydrogen evolving rate was further explored at different pH from 9 to 13, as shown in Figure 2c. The pH value was adjusted by adding either NaOH or HCl into the aqueous solution without affecting the agglomeration of CdS QDs@SMOF assemblies. It was observed that, with the increase of pH value, the H_2-evoluation rate first monotonically increase due to a stronger electrostatic force between CdS QDs and SMOF, and subsequently decrease because of the decreased proton concentration and the possible filling of OH^- into the pores of SMOF. The

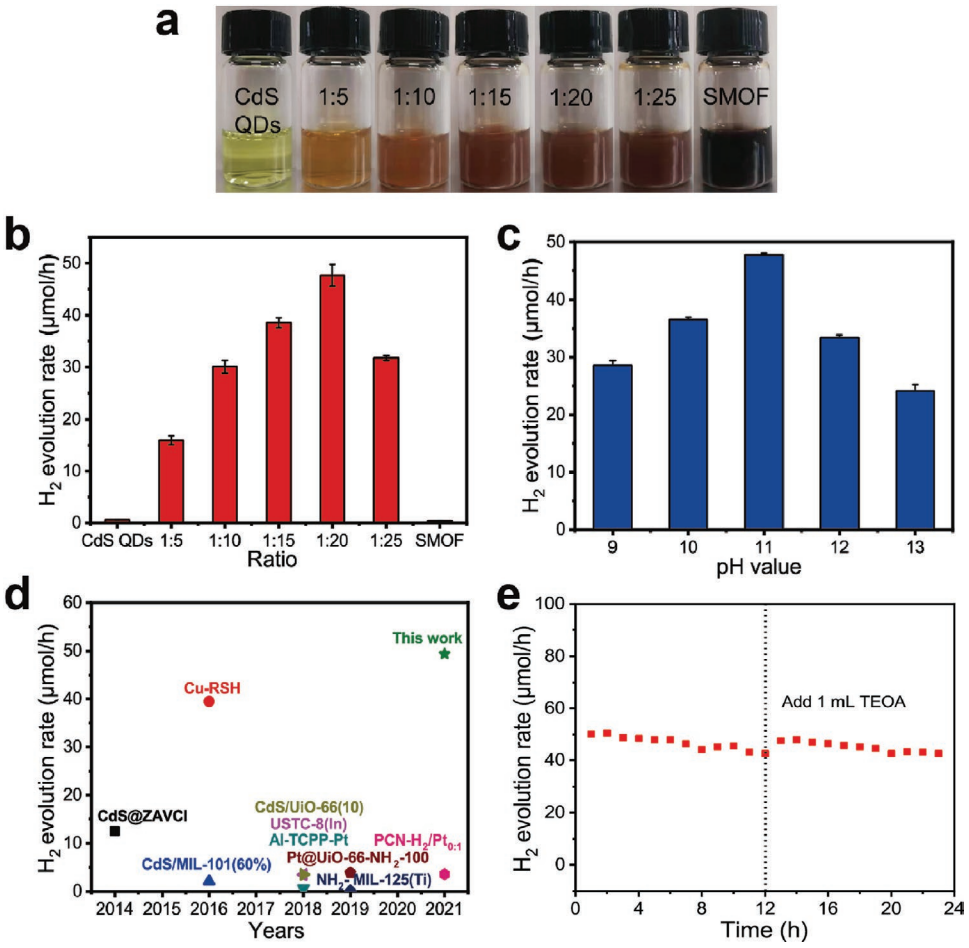

Figure 2. a) The optical images of seven aqueous solution of CdS QDs@SMOF having different mole constitution ratios, which display an increasing absorption from blank CdS QDs to blank SMOF. b) The photocatalytic H_2 evolution activity of CdS QDs@SMOF having varied mole constitution ratios of CdS QDs and SMOF. c) Influence of pH values on the photocatalytic H_2 evolution rate. d) The comparison of photocatalytic H_2 evolution activity of CdS QDs@SMOF with other reported MOFs-based photocatalysts. e) Stability test of CdS QDs@SMOF at a mole constitution ratio of 1:20.

optimized pH value for CdS QDs@SMOF hybrid materials is 11. The impressive production rate renders CdS QDs@SMOF hybrids as one of the most active photocatalysts in the representative MOFs-based photocatalysts (see H_2 evolving rate comparison with previously reported photocatalysts in Figure 2d).[22,23]

Another important criterion for solar energy conversion is the long-term stability of the photoactive composites under actual operating conditions. For the purpose of evaluating the stable performance of CdS QDs@SMOF hybrid materials, longer irradiation was implemented with $[Ru(bpybp)_3]^{2+}$ = 100 μM and 5 μM of CdS QDs (Figure 2e). Notably, the CdS QDs@SMOF hybrid materials show a satisfying photocatalytic stability in a period of 12 h irradiation. The TOF remained unchanged within the first 4 h and then slightly decreased. It is interesting to find that the hybrid structure displayed recoverable activity after adding another 1 mL TEOA and showed good stability during the second 12 h irradiation. Besides, no apparent alteration was observed in TEM image of CdS QDs@SMOF hybrids, in comparison with the pristine counterpart (Figure S7, Supporting Information). These results indicate that the structure of hybrid materials is not altered after the photocatalytic reaction, again confirming the good stability of CdS QDs@SMOF assemblies.

2.3. Proposed Mechanism for the Efficient Photocatalytic Hydrogen Evolution

To understand the mechanism of the CdS QDs@SMOF hybrid materials for highly efficient photocatalytic H_2 evolution, the energy-band diagram was determined. UV–vis diffuse reflectance spectra measurements of the as-prepared samples shows that CdS exhibits an optical absorbance with the edge at 468 nm, while the absorbance of SMOF covers the whole UV–vis region with a broadly intense absorption below 596 nm (**Figure 3**a). The corresponding band gaps for CdS QDs and SMOF were calculated to be 2.65 and 2.08 eV, respectively, according to Tauc plots shown as an inset of Figure 3a. The CdS QDs@SMOF (1:20) hybrid material well inherits the optical features of both CdS and SMOF. The results of Mott–Schottky measurements indicate that the flat band position (V_{fb}) of CdS and SMOF is ≈–0.97 and –0.79 V versus normalized hydrogen electrode (vs NHE), respectively (Figure 3b). As it is generally believed that the bottom of the conduction band (CB) in many *n*-type semiconductors is more negative by ≈0.10 V than the V_{fb},[24] the CB of CdS QDs and SMOF was estimated to be –1.07 and –0.89 V versus NHE,

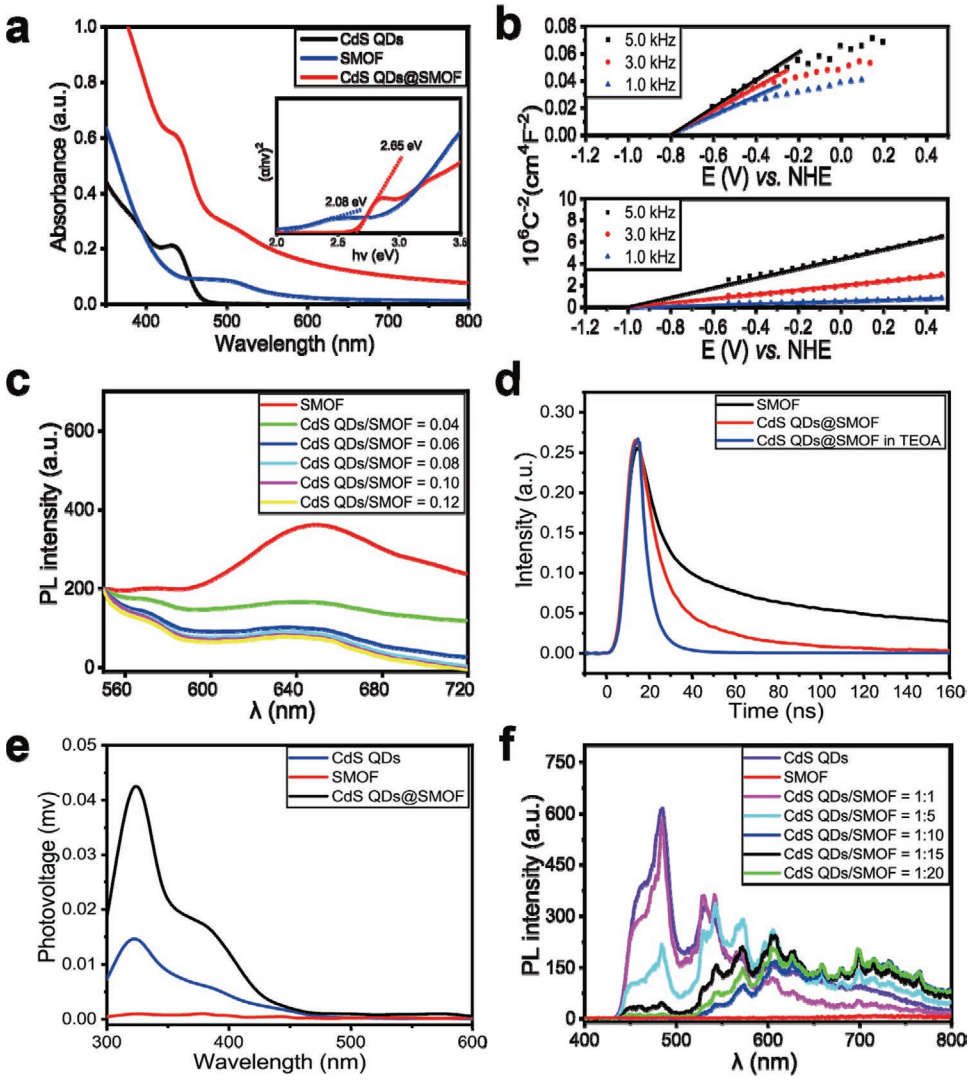

Figure 3. a) UV–vis spectra of CdS QDs, SMOF, and CdS QDs@SMOF. Inset shows the Tauc Plots and band-gap energies. b) Mott–Schottky plots for SMOF (top) and CdS QDs (bottom). c) PL emission spectra of SMOF encapsulating different amounts of CdS QDs under a 450 nm wavelength excitation. d) Transient PL spectra of SMOF and CdS QDs@SMOF under a 450 nm wavelength laser excitation. e) SPV measurement of CdS QDs, SMOF, and CdS QDs@SMOF. f) PL emission spectrum of CdS QDs with different amounts of SMOF adding under a 220 nm wavelength excitation.

respectively. These results prove that CdS QDs and SMOF can both trigger water splitting to produce H_2 as the CBs are more negative than the equilibrium potential of H_2/H^+ (–0.65 V vs NHE, at pH 11). Combined with the band energy, the valence band positions of CdS QDs and SMOF are 1.58 and 1.19 versus NHE, respectively, suggesting that CdS QDs@SMOF (1:20) hybrid material shows a type I junction.

Although forming a type I junction, the enhanced charge separation efficiency can be confirmed by photoluminescence (PL) emission spectra, where the PL intensity of CdS QDs@SMOF hybrid materials is significantly quenched in comparison with that of the parent SMOF (Figure 3c). Almost complete emission quenching for SMOF was observed after adding 0.08 equiv CdS QDs (corresponding to CdS: $[Ru(bpybp)_3]^{2+}$ = 1:12.5), indicating an effective electron transfer between SMOF and CdS in the hybrid materials. We also employed time-resolved emission decay of SMOF before and after CdS incorporation. As shown in Figure 3d, the incorporation of CdS QDs resulted in the average fluorescence lifetime decreasing for SMOF from 73.8 to 31.2 ns based on bi-exponential fits. Furthermore, the average lifetime of SMOF decreased below the instrument response time of ≈7 ns in the presence of TEOA, suggesting that at least over 90% of the excited state was quenched. See the details of fitting procedure in Figure S8, Supporting Information. In addition, surface photovoltage measurement was carried out to investigate the charge separation on the junction interface. As shown in Figure 3e, CdS QDs, SMOF, and CdS QDs@SMOF hybrids all display positive photovoltages, indicating the hole accumulation on the surface of electrodes, which is consistent with the *n*-type semiconductive nature. The photovoltage onset of CdS QDs occurs at 470 nm light irradiation, consistent with the cut-off wavelength in UV–vis spectrum of CdS QDs. Importantly, the surface photovoltage spectroscopy response of CdS QDs@SMOF hybrid material is evidently stronger than both

of SMOF and CdS QDs, suggesting the separation efficiency of photogenerated charges is markedly improved by constructing the heterojunction.[25]

We further tested the PL emission quenching of CdS QDs. When being excited at 220 nm, CdS QDs alone show a strong narrow band-edge emission at 470 nm and a weak broad trap emission at 500–800 nm as demonstrated in Figure 3f, which is consistent with previous reports.[26] We also confirmed SMOF itself has almost no emission according to the red line at 220 nm excitation, indicating that the change of PL emission spectrum is solely attributed to CdS QDs with the addition of SMOF. We observed that after adding 1.0 equiv of SMOF, the band-edge emission for CdS QDs at 470 nm barely changed while the intensity of trap emission at 600–800 nm declined by half. Further arising the SMOF content resulted in a continuous PL intensity decrease of band-edge emission but an increase of trap emission. Interestingly, the trap emission intensity at 700–800 nm reached a maximum when the constitution ratio of SMOF and CdS QDs is 20, consistent with the best photocatalytic activity of CdS QDs@SMOF hybrid materials having a peak activity at CdS QDs: $[Ru(bpybp)_3]^{2+}$ = 1:20. It implies that the introduction of SMOF obviously changes the distribution of photogenerated carriers in excited CdS QDs, and more photogenerated carriers are accumulated at the intrinsic surface defect trap states of CdS QDs for CdS QDs@SMOF (1:20).[27] More importantly, the energy-band position of defect sites is probably very close to the intrinsic CB of CdS QDs, indicating the electron transfer occurred smoothly from trap sites to H^+/H_2.

Given the aforementioned results, we propose a possible mechanism as schematically illustrated in **Figure 4**. From the view point of band structure of CdS QDs and SMOF, a type I heterojunction is expected at their interface, where both CdS QDs and SMOF are excited under solar irradiation. The CdS QDs absorb photons having a wavelength less than ≈420 nm, whereas SMOF is mainly excited at 450–600 nm. Then, SMOF acts as a hole acceptor from adjacent CdS QDs, inhibiting the recombination of photogenerated charges in CdS QDs. Importantly, owing to the interfacial interaction between CdS QDs and SMOF, the interface between SMOF and CdS QDs acts as the trap sites of electrons, resulting in a rapid electron transfer from the CBs of both CdS QDs and SMOF to the trap states and causing an efficient H_2 production, while holes are rapidly quenched by TEOA on SMOF. It should be noticed that the electrostatic attraction between CdS QDs and SMOF shortens the carrier pathway and achieved effective separation of photo-induced electron–hole pairs.

3. Conclusion

We have reported a self-assembly strategy to create the first hybrids of semiconductor QDs and SMOF via electrostatic interaction in water at room temperature. Beyond the periodicity and porosity, the two key features of conventional rigid MOFs, SMOF offers more advantages in the self-assembly because of its changeable pore size and flexible assembly behavior. Efficient encapsulation of CdS QDs in SMOF enables the creation of a novel photocatalytic system that exhibit a H_2 production activity higher than those of reported heterogeneous MOFs-based systems. Detailed examination showed that the CdS QDs@SMOF hybrid (1:20) exhibit an excellent photocatalytic H_2 evolving rate of 49.4 μmol h^{-1} (TOF = 47.0/h), which is ≈80 and 110-folds higher than those of the parent CdS QDs and SMOF, respectively. These results demonstrated that the efficient charge separation across the junction interface in

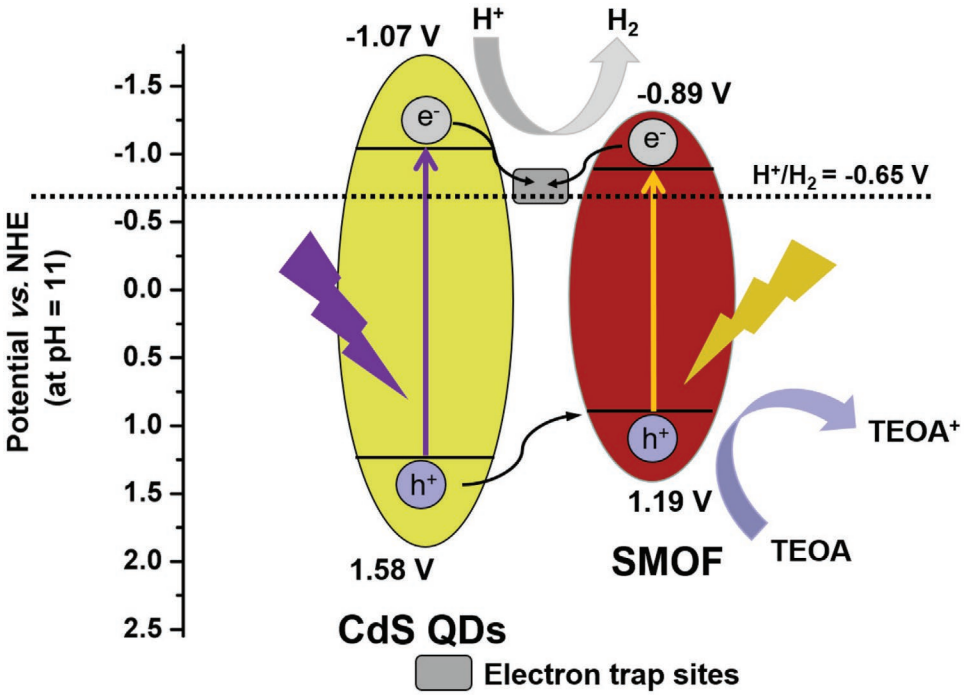

Figure 4. Energy band diagram and mechanism schematic of CdS QDs@SMOF hybrid structure for photocatalytic H_2 evolution.

the hybrid materials greatly contributed to the ultra-high H_2 evolution rate of CdS QDs@SMOF hybrid materials. Our work contributes to a new paradigm for rationally designing photocatalytic systems for the renewable clean energy conversion.

4. Experimental Section

Synthesis of SMOF: The synthesis procedure of SMOF is shown in Scheme S1, Supporting Information.

Compoud-1 to compound-6 were prepared following the procedure reported previously with slight modifications.[19] All reagents were obtained from commercial suppliers and used without further purification unless otherwise noted.

Compound-4: A mixture of compound-3 (1 g, 5.0 mmol) and methyl iodide (3.52 g, 25 mmol) were added to DMF (50 mL), and the mixture was stirred in a sealed tube at 90 °C for 12 h. Tetrabutylammonium chloride (2.78 g, 10.0 mmol) was added into the solution after cooling the mixture to room temperature. The obtained precipitate was filtrated under vacuum, washed with CH_3CN (20 mL) for three times, and dried under a vacuum, after which, a pale white solid (1.2 g, 95%) was obtained. ^{1}H NMR (400 MHz, DMSO-d_6): δ 13.37 (s, 1H), 9.08 (d, J = 6.8 Hz, 2H), 8.56 (d, J = 6.9 Hz, 2H), 8.20–8.14 (m, 4H), 4.36 (s, 3H).

Compound-6: Compound-5 (1.24 g, 4.0 mmol), 4-aminophenylboronic acid pinacol ester (1.92 g, 8.8 mmol), tetrakis(triphenylphosphine) palladium (232 mg, 4.4 mmol), and Na_2CO_3 (2.12 g, 20 mmol) were added into a mixture of DMF (50 mL) and H_2O (25 mL), and were stirred at 120 °C for 12 h. Subsequently, H_2O (50 mL) was added into the mixture. The precipitate was filtrated out after cooling the mixture to the room temperature, and was washed with H_2O (30 mL) and ether. Compound-6 was obtained as a brown solid (1.50 g, 70%). ^{1}H NMR (400 MHz, DMSO-d_6): δ 8.69–8.51 (m, 4H), 7.70–7.55 (m, 6H), 6.70 (d, J = 8.5 Hz, 4H), 5.58 48 (s, 4H).

Compound-2: A mixture of compound-6 (0.51 g, 1.5 mmol), compound-4 (0.84 g, 3.3 mmol), 1-Ethyl-3-(3-dimethylaminopropyl) carbodimide hydrochloride (EDCI, 0.61 g, 3.3 mmol), and N-hydroxybenzotrizole (HOBt, 0.45 g, 3.3 mmol) was added into DMF (50 mL), and stirred in a sealed tube under 100 °C for 24 h. The formed precipitate was filtrated out after cooling to room temperature. Pure compound-2 (0.60 g, 40%) was obtained after recrystallization with DMSO and CH_3CN as an orange or green solid. ^{1}H NMR (400 MHz, DMSO-d_6): δ 10.71 (s, 2H), 9.10 (d, J = 6.7 Hz, 4H), 8.81 (d, J = 5.0 Hz, 2H), 8.77 (s, 2H), 8.62 (d, J = 6.8 Hz, 4H), 8.37–8.19 (m, 8H), 8.07 (d, J = 8.6 Hz, 4H), 7.98 (d, J = 8.7 Hz, 4H), 7.86 (d, J = 5.1, 2H), 4.38 (s, 6H).

Compound-1: After compound-2 (0.2 g, 0.25 mmol) was coordinated to $Ru(DMSO)_4Cl_2$ (0.0384 g, 0.03 mmol) in water (20 mL) at 100 °C, the dark red solution was cooled to room temperature. Then, the solution was treated with acetonitrile (50 mL) to recrystallization, and the target product compound-1 (0.1g, 50 %) was filtered through vacuum filtration as a dark-red solid, followed by washing with 50 mL acetonitrile. ^{1}H NMR (400 MHz, DMSO-d_6): δ 10.70 (s, 6H), 9.09 (d, J = 7.0 Hz, 12H), 8.78 (m, 12H), 8.61 (d, J = 6.8 Hz, 12H), 8.32–8.19 (m, 24H), 8.06 (d, J = 8.6 Hz, 12H), 7.98 (d, J = 8.7 Hz, 12H), 7.86–7.85 (m, 6H), 4.37 (s, 18H).

A mixture of compound-1 (0.1 g, 0.04 mmol) and CB[8] (0.15948 g, 0.12 mmol) was stirred in 60 mL water and then refluxed for 24 h to get a dark-red solution. The crystal of SMOF was obtained by slowly evaporating the dark-red solution in room temperature. The solid crystal of SMOF was obtained by slowly evaporating the dark-red solution in an oil bath at 60 °C.

Synthesis of CdS QDs: The water soluble CdS QDs were prepared by a modified solvothermal method.[28] Typically, CdO (0.28 g; 99%, Aladdin) was added into 1-octadecene (10 mL; >90.0%, Aladdin), and the mixture was stirred and heated to 60 °C, after which oleic acid (1.8 mL; 85%, Aladdin) was injected as a stabilizing ligand. The obtained mixture was vacuumed to remove vapor and oxygen and then heated to 240 °C slowly under a nitrogen atmosphere until CdO was completely dissolved. The obtained light-yellow solution was vacuumed for ≈1 h to remove water at 110 °C. Then, $(NH_4)_2S$ (0.37 mL; 20% in H_2O, Aladdin) dried by freshly activated 3 Å molecular sieve (2.2 g) was dissolved in oleylamine (4 mL; 80–90%, Aladdin), which was injected to $Cd(OA)_2$ precursor in 180 °C for 10 min under stirring and cooled down to the room temperature in a water bath. The product was washed by ethanol (≥95.0%; Sinopharm Chemical Reagent Co., Ltd) and centrifuged at 8000 rpm for 5 min to precipitate. After that, the products were washed by ethanol/hexane ($V_{ethanol}$:V_{hexane} = 2:1) and centrifuged in the same condition one more time. The product was finally dissolved in hexane (≥97.0%; Sinopharm Chemical Reagent Co., Ltd) for the subsequent use.

For phase transfer, mercaptopropionic acid (0.58 mL) was added to ethanol (10 mL) and stirred for a few minutes. Tetramethylammonium hydroxide was added to the solution until the pH was adjusted to 10. The as-prepared CdS-OA hexane solution was mixed with mercaptopropionic acid/ethanol ($V_{mercaptopropionic\ acid}$:$V_{ethanol}$ = 1:20) and stirred vigorously in dark for 2 h. The sublayer solution was washed by acetone (≥99.7%; Sinopharm Chemical Reagent Co., Ltd) and centrifuged at 8000 rpm for 10 min to remove the remaining reagents. After repeated acetone addition and centrifugation twice, the final product was dissolved in deionized water.

CdS-BF_4 was synthesized according to the previous literature with modifications.[28] The as-prepared CdS-OA hexane solution was dried in air and re-dispersed in $CHCl_3$/DMF(V_{CHCl3}:V_{DMF} = 10:1) solution. Trimethyloxonium tetrafluoroborate solution (1.0 M in CH_3CN, Aladdin) was added until the particles precipitated. The prepared mixture was centrifuged at 8000 rpm for 5 min and dried in air. The final obtained particles were re-dispersed in DMF.

Determination of CdS QDs Concentration: The concentration of the CdS QDs was measured through UV–vis spectrum and determined by the equation reported previously.[29]

$$D = -\left(6.6521\times10^{-8}\right)\lambda^3 + \left(1.9557\times10^{-4}\right)\lambda^2 - \left(9.2352\times10^{-2}\right)\lambda + (13.29) \quad (1)$$

$$\varepsilon = 21536(D)^{2.3} \quad (2)$$

$$A = A_m\left(hwhm\right)_{UV}/K \quad (3)$$

$$A = \varepsilon CL \quad (4)$$

where, D(nm) as the average size of CdS QDs was determined by the first exciton absorption peak, λ(nm), in UV–vis absorption spectrum. The molar extinction coefficient (ε) was related to D(nm). The concentration of CdS QDs was calculated using Lambert Beer Law. A and A_m are the calibrated absorbance and the measured absorbance, respectively. $(hwhm)_{UV}$ is the half width at the half-maximum on the long wavelength side of the first absorption peak. K is the average $(hwhm)_{UV}$ of the standard samples used for the measurements. For CdS QDs, the average $(hwhm)_{UV}$ values of the standard samples are 11.

Photocatalytic H_2 Evolution Measurement: The photocatalytic reaction was carried out in a customized quartz cell. A series amount of SMOF was dispersed into a 10 mL TEOA-H_2O solution (V_{TEOA}:V_{H2O} = 1:9) containing CdS QDs (5.0 μM), and the pH value of the mixture was adjusted by adding HCl or NaOH. The system was sonicated for 1 h, and de-aerated by Ar bubbling for 30 min before the photoreaction. Afterward, the system was stirred continuously and irradiated with a solar simulator (Asahi Spectra, HAL-320, output wavelength 350–1100 nm) having a light intensity of ≈100 mW cm^{-2}. The gas products were analyzed with an on-line gas chromatography (Fuli 9790plus) equipped with an MS-5A column and a thermal conductivity detector, using high-purity Ar (99.999%, Shanghai Dumaoai Purified Gas company) as a carrier gas.

TOF of the Catalysts: The TOF of the catalysts was calculated by the following equation:

$$\mathrm{TOF} = \frac{V_{H_2}}{n(\mathrm{catalyst})} \quad (5)$$

where, V_{H_2} is the H_2 evolution rate (mol h^{-1}), n (catalyst) is the mole amount of the catalyst (mol).

STH Conversion Efficiency Calculation: STH was calculated by the following equation:

$$\mathrm{STH} = \frac{V_{H_2} \times \Delta G}{P \times A} \times 100\% \quad (6)$$

where, V_{H_2} is the H_2 evolution rate (mol s^{-1}), ΔG is Gibbs free energy per mol of H_2 (at 25 °C, ΔG = 237.4 kJ mol^{-1}), P (mW cm^{-2}) is the intensity of the irradiation light, and A (cm^2) is the irradiation area.

AQY Calculation: AQY was calculated by the following equation:

$$\mathrm{AQY} = \frac{2R_{H_2} \times N_0}{N} \quad (7)$$

where, R_{H_2} is the H_2 evolution rate (mol s^{-1}), N_0 is Avogadro constant, N is the number of incident photons per second.

Physical Characterizations: The sample morphology was studied by TEM. TEM was carried out using a Tecnai G^2 F20 S-Twin (FEI Company) at 200 kV accelerating voltage. The microscope was equipped with an EDX detector for elemental analysis. ^{1}H nuclear magnetic resonance (NMR) spectra were recorded on a Bruker 400WB Avance III (400 MHz) NMR spectrometer at room temperature. UV–vis characterizations were performed on a Perkin Elmer Lambda 650S UV–vis spectrometer. Optical properties were also studied by PL spectrum (Agilent Cary Eclpse Fluorescence Spectrophotometer with an excitation wavelength of 220 nm for CdS QDs and 450 nm for SMOF). The Mott–Schottky plot was recorded on the Biologic VSP-300 electrochemical workstation in a standard three-electrode system with the photocatalyst-coated FTO as the working electrode, Pt plate as the counter electrode, and a Ag/AgCl as a reference electrode. 0.1 M Na_2SO_4 solution was used as the electrolyte. For SMOF, to prepare the working electrode, the as-synthesized samples (1.0 mg) were added into 1 mL deionized water containing 20 µL Nafion solution (5 wt%), and the working electrodes were prepared by dropping the suspension (60 µL) onto a 1 × 1.5 cm^2 FTO glass substrate electrode surface and dried at room temperature. The transient PL measurements were tested on an assembled device with a Q-smart 450 and Opotek Magic Prism laser, and a Unisoku USP-MD308-PMT-A detector. For detail, quartz reaction cell sealed with rubber stopper containing 4 mL SMOF (1×10^{-5} M) and 4 mL CdS (5×10^{-6} M)@SMOF (1×10^{-5} M) was bubbled with N_2 for 1.0 h respectively, then excited by laser with an excitation wavelength of 450 nm.

The SPV measurement was carried out based on the lock-in amplifier. And the SPV spectra in the experiments were measured as the in-phase signals (Uxsignal). Herein, the measurement system consisted of a source of monochromatic light, a lock-in amplifier (SR830, Stanford Research Systems, Inc.) with a light chopper (SR540, Stanford Research Systems, Inc.), and a sample chamber. The monochromatic light was provided by a 500 W xenon lamp and a monochromator (SBP500, Zolix), which was chopped with a frequency of 23 Hz.

The SAXS data were collected on BL19U2 at the Shanghai Synchrotron Radiation Facility with a wavelength of 0.1033 nm (energy 12 keV) and a beam size of 0.30 × 0.05 (H × V) mm^2. A cylindrical quartz glass capillary of 1.5 mm diameter with a peristaltic flow cell was used for automatically sample mounting. An evacuated flight tube was used to cover the sample-to-detector distance of 2.21 m. A motorized beam stop was placed inside the flight tube. A Dectris Pilatus 1 M Detector (172 × 172 µm pixel size) was used. The exposure time was 0.5 s for each sample. 1D scattering–intensity profiles $I(q)$ were obtained from circularly averaging the 2D scattering patterns and the corresponding structure factors $S(q)$ for the studied structures: $q = 4\pi\sin\theta/\lambda$, where 2θ is the scattering angle and λ is the wavelength of the X-ray.

Supporting Information

Supporting Information is available from the Wiley Online Library or from the author.

Acknowledgements

C.P. and J.C. contributed equally to this work. This research was supported by National Natural Science Foundation of China (Grants 21872039, 21974027, and 22072030) and Science and Technology Commission of Shanghai Municipality (Grants 18JC1411700 and 19DZ2270100).

Conflict of Interest

The authors declare no conflict of interest.

Data Availability Statement

Research data are not shared.

Keywords

heterostructures, hydrogen generation, photocatalysis, quantum dots, supramolecular metal organic frameworks

Received: September 3, 2021
Revised: October 12, 2021
Published online: November 25, 2021

[1] K. W. Barnham, M. Mazzer, B. Clive, *Nat. Mater.* **2006**, *5*, 161.
[2] Y. Tachibana, L. Vayssieres, J. R. Durrant, *Nat. Photonics* **2012**, *6*, 511.
[3] Z. Wang, C. Li, K. Domen, *Chem. Soc. Rev.* **2019**, *48*, 2109.
[4] K. Sordakis, C. Tang, L. K. Vogt, H. Junge, P. J. Dyson, M. Beller, G. Laurenczy, *Chem. Rev.* **2018**, *118*, 372.
[5] S. Chen, T. Takata, K. Domen, *Nat. Rev. Mater.* **2017**, *2*, 17050.
[6] N. S. Lewis, *Science* **2016**, *351*, aad1920.
[7] Q. Wang, T. Hisatomi, Q. Jia, H. Tokudome, M. Zhong, C. Wang, Z. Pan, T. Takata, M. Nakabayashi, N. Shibata, Y. Li, I. D. Sharp, A. Kudo, T. Yamada, K. Domen, *Nat. Mater.* **2016**, *15*, 611.
[8] L. Wang, M. Cai, W. Sun, L. He, X. Zhang, *Adv. Mater. Interfaces* **2018**, *5*, 1701694.
[9] Y. Wang, H. Suzuki, J. Xie, O. Tomita, D. J. Martin, M. Higashi, D. Kong, R. Abe, J. Tang, *Chem. Rev.* **2018**, *118*, 5201.
[10] a) B. Chen, M. Eddaoudi, S. T. Hyde, M. Keeffe, O. M. Yaghi, *Science* **2001**, *291*, 1021; b) H. Li, M. Eddaoudi, M. O'Keeffe, O. M. Yaghi, *Nature* **1999**, *402*, 276.
[11] X. Ma, L. Wang, Q. Zhang, H. L. Jiang, *Angew. Chem., Int. Ed.* **2019**, *58*, 12175.
[12] S. Tasleem, M. Tahir, W. A. Khalifa, *Int. J. Hydrogen Energy* **2021**, *46*, 14148.
[13] R. Freund, O. Zaremba, G. Arnauts, R. Ameloot, G. Skorupskii, M. Dincă, A. Bavykina, J. Gascon, A. Ejsmont, J. Gościańska, M. Kalmutzki, U. Lächelt, E. Ploetz, C. Diercks, S. Wuttke, *Angew. Chem., Int. Ed.* **2021**, https://doi.org/10.1002/ange.202106259.
[14] H. L. Tang, X. J. Sun, F. M. Zhang, *Dalton Trans.* **2020**, *49*, 12136.
[15] X. Yang, D. Wang, *ACS Appl. Energy Mater.* **2018**, *1*, 6657.
[16] M. R. di Nunzio, E. Caballero-Mancebo, B. Cohen, A. Douhal, *J. Photochem. Photobiol., C* **2020**, *44*, 100355.
[17] L. Yang, X. Tan, Z. Wang, X. Zhang, *Chem. Rev.* **2015**, *115*, 7196.
[18] a) J. Tian, T. Y. Zhou, S. C. Zhang, S. Aloni, M. V. Altoe, S. H. Xie, H. Wang, D. W. Zhang, X. Zhao, Y. Liu, Z. T. Li, *Nat. Commun.* **2014**, *5*, 5574; b) K. D. Zhang, J. Tian, D. Hanifi, Y. Zhang, A. C. H. Sue, T. Y. Zhou, L. Zhang, X. Zhao, Y. Liu, Z. T. Li, *J. Am. Chem. Soc.* **2013**, *135*, 17913.
[19] J. Tian, Z. Y. Xu, D. W. Zhang, H. Wang, S. H. Xie, D. W. Xu, Y. H. Ren, H. Wang, Y. Liu, Z. T. Li, *Nat. Commun.* **2016**, *7*, 11580.

[20] H. Zhang, B. R. Hyun, F. W. Wise, R. D. Robinson, *Nano Lett.* **2012**, *12*, 5856.
[21] a) Y. Gao, K. Liu, R. Kang, J. Xia, G. Yu, S. Deng, *J. Hazard. Mater.* **2018**, *359*, 248; b) J. Cui, N. Gao, X. Yin, W. Zhang, Y. Liang, L. Tian, K. Zhou, S. Wang, G. Li, *Nanoscale* **2018**, *10*, 9192; c) L. Y. Wu, Y. F. Mu, X. X. Guo, W. Zhang, Z. M. Zhang, M. Zhang, T. B. Lu, *Angew. Chem., Int. Ed.* **2019**, *58*, 9491.
[22] a) S. Saha, G. Das, J. Thote, R. Banerjee, *J. Am. Chem. Soc.* **2014**, *136*, 14845; b) X. Y. Dong, M. Zhang, R. B. Pei, Q. Wang, D. H. Wei, S. Q. Zang, Y. T. Fan, T. C. Mak, *Angew. Chem., Int. Ed.* **2016**, *55*, 2073; c) Y. Wang, Y. Zhang, Z. Jiang, G. Jiang, Z. Zhao, Q. Wu, Y. Liu, Q. Xu, A. Duan, C. Xu, *Appl. Catal., B* **2016**, *185*, 307; d) X. Fang, Q. Shang, Y. Wang, L. Jiao, T. Yao, Y. Li, Q. Zhang, Y. Luo, H. L. Jiang, *Adv. Mater.* **2018**, *30*, 0935.
[23] a) F. Leng, H. Liu, M. Ding, Q. P. Lin, H. L. Jiang, *ACS Catal.* **2018**, *8*, 4583; b) F. Guo, J. H. Guo, P. Wang, Y. S. Kang, Y. Liu, J. Zhao, W. Y. Sun, *Chem. Sci.* **2019**, *10*, 4834; c) C. Lin, C. Han, H. Zhang, L. Gong, Y. Gao, H. Wang, Y. Bian, R. Li, J. Jiang, *Inorg. Chem.* **2021**, *60*, 3988.
[24] a) A. Ishikawa, T. Takata, J. N. Kondo, M. Hara, H. Kobayashi, K. Domen, *J. Am. Chem. Soc.* **2002**, *124*, 13547; b) J. Zhang, X. Chen, K. Takanabe, K. Maeda, K. Domen, J. D. Epping, X. Fu, M. Antonietti, X. Wang, *Angew. Chem.* **2010**, *49*, 441.
[25] S. W. Verbruggen, J. J. Dirckx, J. A. Martens, S. Lenaerts, *Catal. Today* **2013**, *209*, 215.
[26] a) D. Kim, S. Okahara, K. Shimura, M. Nakayama, *J. Phys. Chem. C* **2009**, *113*, 7015; b) L. Hu, C. Ma, G. Chen, Z. Zhu, *J. Lumin.* **2020**, *220*, 0022.
[27] a) A. Veamatahau, B. Jiang, T. Seifert, S. Makuta, K. Latham, M. Kanehara, T. Teranishi, Y. Tachibana, *Phys. Chem. Chem. Phys.* **2015**, *17*, 2850; b) S. Li, D. Meng, L. Hou, D. Wang, T. Xie, *Appl. Surf. Sci.* **2016**, *371*, 164.
[28] Q. Q. Bi, J. W. Wang, J. X. Lv, J. Wang, W. Zhang, T. B. Lu, *ACS Catal.* **2018**, *8*, 11815.
[29] W. W. Yu, L. Qu, W. Guo, X. Peng, *Chem. Mater.* **2003**, *15*, 2854.